Development of Turbidity Monitoring Methods Over the Coastal Zone Using Aerial Drone : Case Study in the Estuary of Tokoro, Hokkaido, Japan, After Low Pressure Events

By

Koji Asakuma[*][†], Chihiro Omiya[*], Naoto Kida[*] and Mitsuaki Kitamura[**]

Summary : The coastal area of Hokkaido bordering the Sea of Okhotsk is famous for cultivating scallops, however, there have been problems of damage to scallops caused by suspended solids supplied from rivers flowing through these areas after low pressure events ; therefore, the development of a simple and wide-range monitoring method for suspended solids is required. This study aimed to develop a turbidity monitoring method using only an aerial drone, that does not require a special device, targeting the estuary of the Tokoro River flowing through the Tokoro Town located in east Hokkaido. The specifications of commercially available cameras for use by general customers are often not disclosed ; thus, when using such cameras for measurements, it is necessary to analyze their specifications in relation to the object of measurement. The relationship between the turbidity of the turbid water sampled in the estuary of Tokoro River and the reflectance calculated from the images of the river surface photographed with the hovering drone at the site of water sampling were compared using a linear regression model and an exponential regression model. The drone mounted camera detected turbidity with high reliability when using the exponential regression model. As a result of comparing the Root Mean Square Error (RMSE) of both models, the camera mounted on this drone was found to have high reproducibility of high turbidity when using an exponential regression model. However, the precision of this model is slightly insufficient for routine monitoring for daily condition of the river with low turbidity. Thus, improvements such as simultaneous observation of phytoplankton other than inorganic suspended solids are necessary.

1.　Introduction

The coastal area of Hokkaido bordering the Sea of Okhotsk is famous for its prosperous fisheries. The fisheries catch of the foreshore adjacent to the Sea of Okhotsk reaches 379,000 t per year. The major fishery species captured in this coastal area include scallop (63.6%), salmon (11.4%), and arabesque greenling (9.7%)[1]. Because scallops are benthic, growing in fixed coastal areas until harvesting, a locally stable food source is required. Scallops tend to feed on phytoplankton, which are primary producers in the sea, with productivity being driven by the surrounding environment[2]. Thus, to main-tain the high productivity of phytoplankton in fixed areas, high concentrations of nutrients are required. The coastal area of the Sea of Okhotsk from winter to spring is occupied by the nutrient-rich Okhotsk surface water. However, the nutrient poor Soya warm current flows through these coastal area from early summer to late autumn, from the coast of Hokkaido to nearly 40 km offshore[3-6]. For example, during summer, nitrates in the offshore waters (more than 74 km from the coast) exceed 20 μM, whereas nitrates in the Soya warm current are just 2 μM or less[7]. The area offshore from Tokoro Town, which is an important fishing area for scallops (Figure 1), has also been filled by the Soya warm water from June

[*] Department of Aquatic Bioscience, Faculty of Bioindustry, Tokyo University of Agriculture
[**] Department of Aquatic Bioscience, Graduate school of Bioindustry, Tokyo University of Agriculture
[†] Corresponding author (E-mail : k-asakum@bioindustry.nodai.ac.jp)

onwards[7]. Therefore, for phytoplankton to grow off-shore from Tokoro after June, a different nutrient source must be supplied to the water mass influenced by the Soya warm current other than the intermediate cold water. For instance, Tokoro River flows through Tokoro Town and supplies an alternative source of nutrients. Tokoro River is the largest river on the coast of east Hokkaido that flows into the Sea of Okhotsk. The catchment basin of this river is 1,930 km^2, and the average flow rate is 26.41 m^{3}s^{-1} [8]. Materials supplied from rivers include both nutrients and organic and inorganic suspended solids, with Tokoro River being no exception.

These organic and inorganic suspended solids are preyed on directly by filter feeding bivalves, such as scallops, that inhabit the benthic substrate. Part of the suspended solids is digested and assimilated in the gastrointestinal tract of bivalves, while the remaining organic matter is excreted as feces and the inorganic suspended material is excreted as fake feces. The physical strength of bivalves is weakened by the excretion of fake feces[9]. It was confirmed that the ciliary movement of the gill of scallops is noticeably suppressed by suspension containing 0.05% (about 500 degrees in terms of turbidity) mud in sea water[10].

Typhoons and explosive cyclones occur under conditions of low pressure, and have occurred with greater frequently in recent years[11-13]. Consequently, there is concern about scallops being suffocated by increased concentrations of sediments flowing out of rivers in the coastal area of Hokkaido in the Sea of Okhotsk following such events[14, 15]. However, it is difficult to establish the extent of damage caused by low pressure weather events in the coastal area of the Sea of Okhotsk. Yet, the municipalities and fisheries community in this area need to implement methods for estimating damage to the coastal area following such events[16]. Beside sediments flowing out from rivers there may also be drifted sediments generated by the rolling up from the seafloor due to waves caused by strong wind, but it is reported that there is almost no impact while the river water is increasing[17, 18]. In the case of steady state of the river, there is also the influence of sedimentation of drifted sediments from the seafloor, but this study does not treat it because the study is targeted at the time of river water increases.

Observation of plumes of suspended solids from Tokoro River and estuary using satellite images in our previous study showed that the plume spreads about 8 km eastwards[19]. However, because visible to near infrared wavelengths were used to observe suspended solids, satellite imagery is susceptible to the influence of clouds. In particular, the turbidity of river suspended matter may be instantaneously high during typhoons and explosive
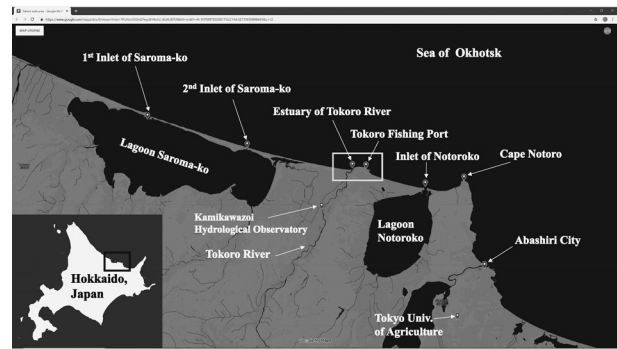

Fig. 1   Map of Tokoro coastal area on the eastern part of Hokkaido coast bordering the Sea of Okhotsk.
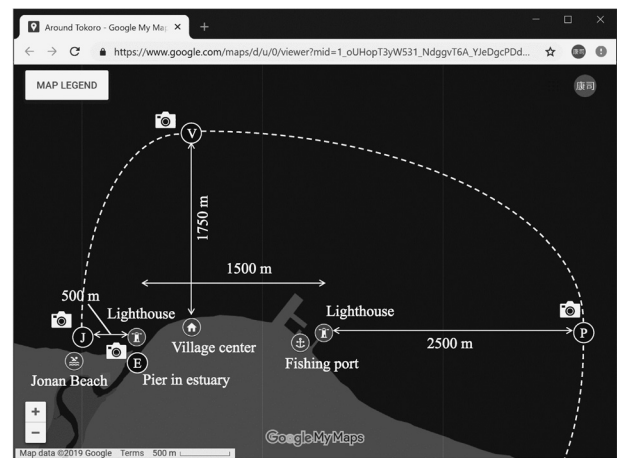

Fig. 2   Enlarged map of the estuary of Tokoro River, representing the gray square presented in Figure 1. The drone was launched and landed at the piers in the estuary of Tokoro River, Tokoro Fishing Village Center and Tokoro Fishing Port. The camera icon shows the photographed point using the drone. The dotted line shows a tidal boundary line predicted from the drone image.

cyclones. Because clouds develop during such events, it is not possible to capture that moment or immediate aftermath of the event with satellite imagery. Sometimes, clouds temporarily clear shortly after typhoons or gales stop blowing, however there is a very low probability of the satellite passing through at that moment. Furthermore, even if the wind subsides, the waves on the coast remain high, making it difficult to observe turbidity from a fishing boat.

In recent years, drones (or Unmanned Aerial Vehicle, UAV) have been effectively used to establish the situation following natural disasters, including volcanic eruptions[20, 21], earthquakes, and landslides[22]. Drones fly at low altitudes above the ground, but below the clouds, compensating for satellite observations ; thus, this approach could be used as a substitute for satellite imaging. For oceanic

and coastal areas, problems remain, including battery duration and susceptibility to weather ; however, high precision observations with drones are possible through the installation of hyperspectral cameras or high resolution cameras[23, 24]. For instance, high performance rotary wing type drones with a resolution of 4 K or more are now available at relatively low costs. These drones are equipped with GPS and autonomous navigation systems, allowing them to fly under certain wind conditions with no problems, and even beginners can easily operate them. It is possible to photograph aerial images showing how plumes spread from the mouth of rivers around coastal areas with drones, even when cloud cover is heavy following the passing of typhoons, as long as the wind is not strong. However, drones developed specifically for sensing are still expensive; low cost drones for beginners are equipped with a CCD camera for general customers. Although CCD cameras for general customers are designed to look vivid with human eyes[25], their specifications are not disclosed, and in many cases the specifications for observation objects are not known. This technique of making the camera image look vivid is implemented with an exponential curve called the γ correction[25]. Therefore, to use low cost drones for observations, it is first required to find a calibration method and the value of γ.

This study aimed to estimate the amount of suspended solids flowing from the estuary of Tokoro River following the passing of a typhoon, in addition to estimating the amount of suspended solids that settled in the coastal area offshore of Tokoro Town, using a low cost drone with an installed aerial camera and no special equipment.

2. Materials and Study sites

2.1 Measurement of the outflow range of suspended solid from the estuary of Tokoro River

To measure the outflow range of suspended solids from Tokoro River, sea surface reflectance was calculated from images photographed with a drone. These aerial images were obtained using a DJI Phantom 4. To convert the photographic images to sea surface reflectance, a standard white board with 99% Lambertian reflectance (Labsphere Inc.) was photographed before the flight, and this white board photographed again after the flight. Figure 2 presents a map of the estuary of Tokoro River. The drone was launched and landed at the piers in the estuary of Tokoro River, Tokoro Fishing Village Center and Tokoro Fishing Port. The lighthouse in the estuary of Tokoro River, the Tokoro Jonan Beach, the lighthouse in Tokoro Fishing Port, the Breakwater of the Lake Inlet of Lagoon Notoro-ko and Cape Notoro were photographed as landmarks. The area of the plume on the surface was measured using the GPS system onboard the drone

combined with positional information of landmarks on the map. The tidal boundary information was separated from the sea surface color of the drone RGB images (e.g., blue color of the ocean sea surface or brown color of turbid water from the river).

Aerial imagery using the drone was collected on October 24, 2017, immediately after Typhoon Lan (Typhoon No. 21), and October 27, three days after the typhoon, when conditions had calmed down. On October 31, 2017, only water surface imagery of the river was obtained with hovering of the drone because the wind speed exceeded $7\,\mathrm{m\,s}^{-1}$ due to the low pressure developed in the Sea of Okhotsk. To document the steady state of the estuary, water surface imagery was obtained on September 28, 2017, December 4, 2017, April 13, 2018 and April 20, 2018 by hovering the drone. Thus, aerial imagery was obtained with the hovering of the drone, from which the turbidity and water surface reflectance of the estuary were measured.

2.2 Measurement of turbidity, sedimentation rate and particle size of suspended solids

To determine the amount of actual suspended solids flowing out from Tokoro River, the surface water of the estuary of the river was sampled with a hydrochloric acid washed bucket, in accordance with the drone flight. The sampled water was analyzed with a transmitted beam type digital color turbidimeter, WA-PT-4DG (Kyoritu Chemical Check Lab., Corp.), calibrated with polystyrene particles. The dry weight concentration was measured for water sampled on October 31, 2017, December 4, 2017, April 13, 2018 and April 20, 2018. A total of 500 mL turbid water was passed through the Whatman GF/F filter, then the dry weight was weighted from the difference in weight of the filter before and after filtration.

The sedimentation rate was measured using river water sampled on October 31, 2019. The sampled water was dispensed in a 500 mL graduated cylinder (45 cm height). Then, 10 mL water on the surface was sampled with an auto pipette. The turbidity of surface water was measured with a digital color turbidity meter. Turbidity was measured at set time intervals until 2 degrees turbidity was reached[26]. This value (2 degree turbidity) is the costal revetment standard in Japan that is assumed not to affect coastal fisheries. According to the environmental standards of rivers in Japan, the turbidity of less than 25 degrees is not considered to impact river water quality[27].

The particle size of the suspended solids was measured using river water sampled on the same day to measure the sedimentation rate. The sampled water was poured

in a 500 mL graduated cylinder that was prepared separately to that used to measure the sedimentation rate. After allowing the sample to stand for 20 days, supernatant water was gently discharged with a tube and concentrated to 25 mL. Then, 0.5 mL of this concentrated water sample was pipetted out with a micro pipette and the number of particles for each particle size was counted with a biological microscope (Olympus CX41 Upright Microscope). A 0.5 mL volume of the concentrated water sample was fractionated by 1,000 fractions. The size of each fraction was 5 μm square. The number of particles in each fraction was 524. One-hundred particles were randomly selected, and particle size was measured.

3. Results

3.1 Influence range of turbid water from the mouth of Tokoro River

Figure 3 shows a situational view photographed with the drone of the estuary of the Tokoro River on October 24, after Typhoon Lan passed through. The tidal boundary between the density of the turbid river water and the density of the clear seawater was visually confirmed by flying the drone on the west side and north side of the lighthouse (Point E in Figure 2 ; Figure 3), and was located near Tokoro Public Pool on Jonan Beach 500 m west of the lighthouse (Point J in Figure 2 ; Figure 4) and 1750 m north of the fishing village center (Point V in Figure 2). By turning the drone towards the tidal boundary line, this boundary line seemed to draw a clean arc without interruption. Likewise, the tidal boundary line was delineated 2,500 m on the east side of Tokoro Fishing Port, before the inlet of Lagoon Notoro-ko (Point P in Figure 2 ; Figure 5). Thus, suspended solids existed on the sea surface for about 5 km in a west to east direction from 500 m west of the estuary (Point J in Figure 2) to 2500 m east of the Fishing Port (Point P in Figure 2), and 1750 m in a south to north direction from the Fishing Village Center to 1750 m north of this center (Point V in Figure 2). The Nadia image over each tidal boundary line on October 24 is shown in Figure 6, and a similar image on October 27 is shown in Figure 7. Compared to Figure 6, the contrast between the inside and the outside of the boundary line clearly decreased.

3.2 Calculating turbidity from drone imagery

Figure 8 is the aerial picture of the work scenery of surface water sampling photographed with the drone on October 24, 2017. The square area over the river surface and the standard white board image were cropped to 100×100 pixels from Figure 8 to obtain each pixel value. Nine of the pixel values of the Tokoro river estuary image were divided by the pixel values of the white

Fig. 3 Situational view of the estuary of Tokoro River photographed with the DJI Phantom 4 on October 24, 2017.
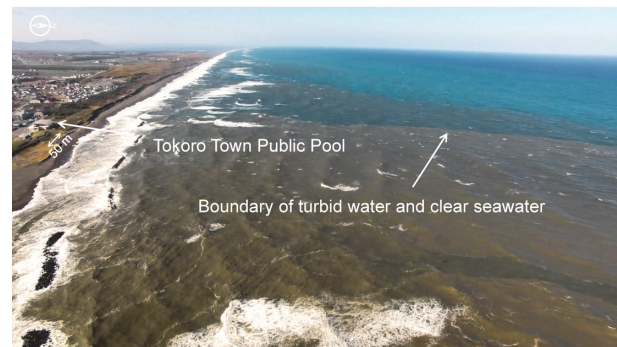

Fig. 4 Image of the tidal boundary between turbid water and seawater fronting Tokoro Town Public Pool at Tokoro Jonan Beach on the west side of the estuary of Tokoro River on October 24, 2017.
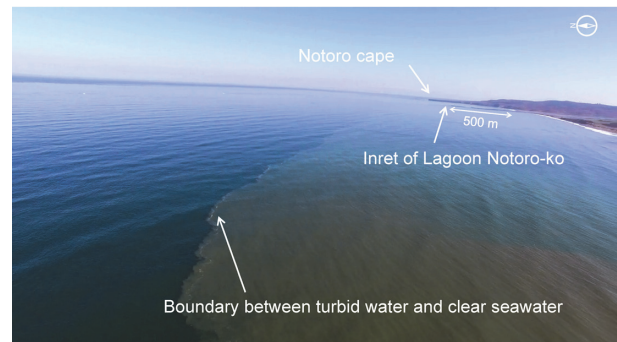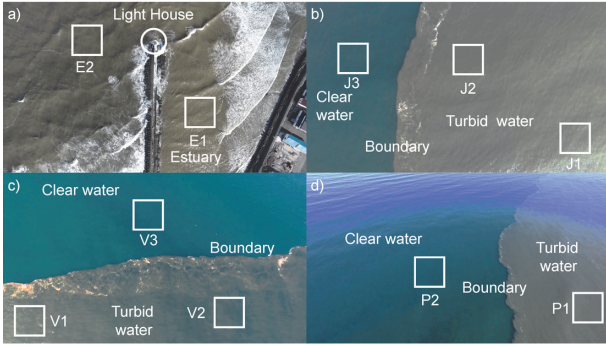

Fig. 5 Image of the boundary between turbid water and seawater at the Inlet of Lagoon Notoro-ko Tokoro on the east side of Tokoro Fishing Port on October 24, 2017.

board, and were then multiplied by 255 to obtain 8-bit normalized imagery (Hereinafter, all the pixel values indicate normalized values). Histograms were created from the R, G, and B channel images cut into squares from Figure 8 ; These histograms are shown in Figure 9. The average pixel value of each R, G, and B channel in Figure 8 was 132.4 ± 3.9, 116.5 ± 3.9, and 89.7 ± 3.8, respectively. In comparison, turbidity based on the turbidimeter

Fig. 6 Image showing the nadir view near the tidal boundary line between turbid water and clear seawater on October 24, 2017. a) Above the estuary. b) Offshore from Tokoro Jonan Beach. c) Offshore from Tokoro Fishing Village Center. d) East side of Tokoro Fishing Port, near the Lagoon Notoro-ko inlet. Squares in the figure were used as test site to calculate turbidity.
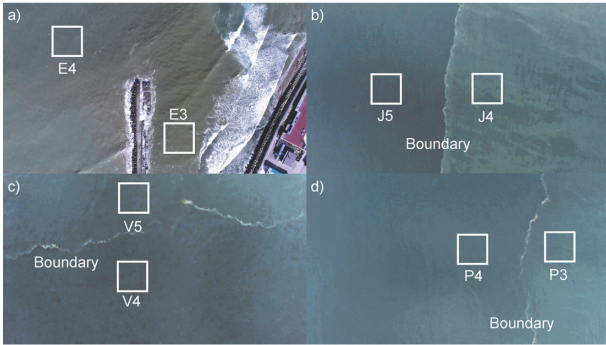

Fig. 7 Drone image of the nadir on October 27, 2017, obtained at the same place as in Figure 6.

**Fig. 8** Drone image when sampling surface water on October 24, 2017.

of the water sampled on the estuary surface on this day was 60.0 degrees. All average normalized pixel values for R, G, and B are presented as x_R, x_G, and x_B, respectively. The turbidity observed with the turbidimeter is represented by τ, while the turbidity based on the ratio of the dry weight of the suspension in 1 L water is represented by w. Table 1 presents the x_R, x_G, and x_B obtained from
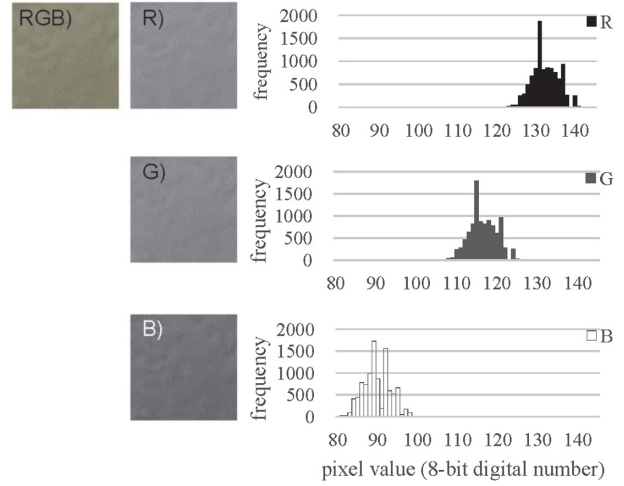
Fig. 9 RGB Composed image and each image of the R, G, and B channels and each histogram based on the white square shown in Figure 8.

Table 1 Average normalized pixel values of x_R, x_G, and x_B for each R, G, and B channel obtained from the drone, turbidity τ, and dry weight turbidity w.

date	place	turbidity from turbidimeter	dry weight turbidity	average pixel value		
		τ	w	x_R	x_G	x_B
2017/9/28	estuary	8.9	---	101.9 ± 1.8	112.9 ± 1.3	105.4 ± 1.8
	port	0.6	---	103.8 ± 2.6	112.2 ± 2.4	112.0 ± 2.4
2017/10/24	estuary	60.0	---	132.4 ± 3.9	116.5 ± 3.9	89.7 ± 3.8
2017/10/27	estuary	2.4	---	54.5 ± 2.8	96.3 ± 2.1	83.0 ± 3.2
	port	3.7	---	108.2 ± 5.5	113.1 ± 6.1	86.9 ± 6.0
2017/10/31	estuary	64.3	129.0	138.9 ± 9.4	123.7 ± 8.4	105.9 ± 6.6
2017/12/4	estuary	1.9	2.4	67.9 ± 1.5	92.0 ± 1.8	66.7 ± 1.4
2018/4/13	estuary	34.6	51.6	123.6 ± 2.7	122.1 ± 3.1	97.7 ± 5.9
2018/4/20	estuary	33.5	47.8	120.8 ± 4.5	119.7 ± 5.1	94.2 ± 7.7
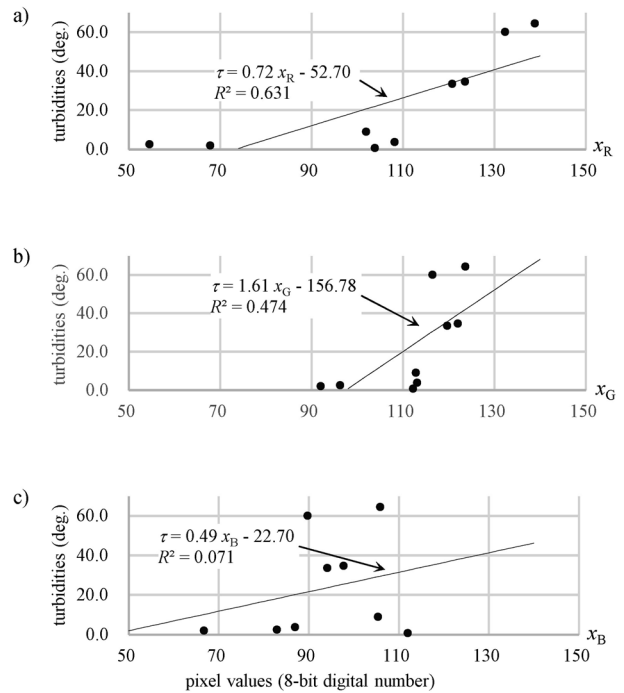
Fig. 10 Relationship between x_R, x_G, x_B and τ presented in Table 1. Solid line shows the regression line between the pixel values and τ. a) R channel, b) G channel and c) B channel.

the drone images using the same method on October 24, and τ and w obtained by water sampling during the observation period. The highest τ during this period was 64.3 degrees in the estuary, which was recorded on October 31, just after the low pressure from the Sea of Okhotsk. The x_R, x_G, and x_B were 138.9 ± 9.4, 123.7 ± 8.4, and 105.9 ± 6.6, respectively, on this date. The lowest τ was 0.6 degrees in the port on September 28. The x_R, x_G, and x_B were 103.8 ± 2.6, 112.2 ± 2.4, and 112.0 ± 2.4, respectively, on this date. Regression lines were calculated from relationships between each x_R, x_G, and x_B and τ from Table 1. These regression lines are shown in Figure 10. The regression formula of x_R and τ was expressed as :

$$\tau = 0.72 x_R - 52.70 \ (R^2 = 0.631, \ P < 0.01) \cdots (1).$$

The root means square error (RMSE)[28] is often used to indicate precision in remote sensing (rather than the standard deviation), and was $RMSE = 14.69$ when applying formula (1). The regression formula of x_G was expressed as :

$$\tau = 1.61 x_G - 156.78 \ (R^2 = 0.474, \ P < 0.05) \cdots (2).$$

The RMSE in formula (2) was $RMSE = 17.54$. The regression formula of x_B was :

$$\tau = 0.49 x_B - 22.70 \ (R^2 = 0.071, \ P = 0.49 > 0.05) \cdots (3).$$

Thus, x_B showed little correlation with τ. Based on these results, x_B was excluded from the subsequent discussion. The estimated value of τ was expressed as a function of the linear combination of x_R and x_G :

$$\tau = a_R x_R + a_G x_G + b. \cdots (4)$$

The optimal parameter found by the least squares method using MS-Excel's solver by placing τ, x_R and x_G in Table 1 to formula (1) was $a_R = 0.987$, $a_G = -0.674$ and $b = 0.060$. However, since a_G became negative, the multiple regression analysis of τ and x_R, x_G was performed. The P value for x_R in this analysis was 0.01, but the P value for x_G was $0.3 > 0.05$. This result indicates the confidence interval of x_G contains 0.

Next, to suppress the vivid correction for the camera, the method of estimation was modified from the linear combination regression to exponential curve regression. Since this suppression correction is expressed by the inverse operation of gamma correction, so the corrected x_R' is expressed with the pixel value x_R and the parameter of gamma correction for R channel γ_R :

$$x_R' = 255 \left(\frac{x_R}{255} \right)^{\frac{1}{\gamma_R}}.$$

Using this corrected pixel value in R channel with the regression parameters c_R and d_R, rewriting the regression equation for τ can be expressed as :
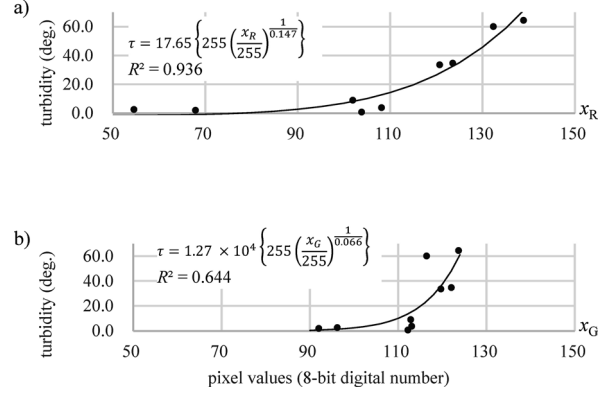

a)

b)

Fig. 11 Relationship of the γ corrected x_R and x_G with τ.
a) R channel, b) G channel.

$$\tau = c_R \left\{ 255 \left(\frac{x_R}{255} \right)^{\frac{1}{\gamma_R}} \right\} + d_R. \cdots (5)$$

Figure 11 shows the relationship for the γ corrected pixel values of x_R and x_G with τ. In the curve shown in Figure 11, the determination coefficient $R^2 = 0.936$ was maximized when $\gamma_R = 0.147$, $c_R = 17.65$ and $d_R = 0.0$. The P value was $P < 0.01$ and $RMSE = 2.04$ at this case. Similarly, by replacing c_R, x_R, γ_R and d_R with c_G, x_G, γ_G and d_G respectively in the curve shown in Figure 11 b), the determination coefficient $R^2 = 0.936$ was maximized when $\gamma_G = 0.066$, $c_G = 1.27 \times 10^4$, $d_G = 0.0$, $P < 0.01$ and $RMSE = 4.81$.

3.3 Relationship between turbidity τ measurements based on the turbidimeter and the dry weight turbidity w of suspended solids

The turbidity τ obtained with the turbidimeter was an optically relative value determined from the polystyrene standard. To quantitatively evaluate the inflow of various suspended substances contained in river water, it must be converted to the weight of the actually flowing suspended solids. Figure 12 shows the relationship between τ obtained with the turbidimeter and the dry weight turbidity w of the suspended solids in sampled water (shown in Table 1). The solid dotted line in this Figure shows the linear regression formula :

$$w = 2.02 \tau - 10.09 \ (R^2 = 0.961, \ P = 0.02 < 0.05) \cdots (6).$$

The τ estimated from the drone using formula (5) was converted to w of suspended solids using this formula (6).

3.4 Estimation of sedimentation rate of suspension

The number of particles of the sampled water in the estuary of the Tokoro river counted with the microscope is shown in Table 2. Assuming that the number of particles $N(D)$ follows a bi-modal normal distribution of particle diameter D in the sampled water, this particle distribution could be expressed as :
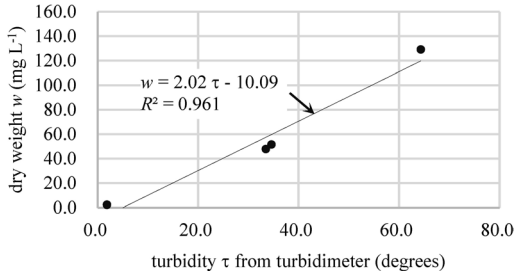
Fig. 12 Relationship between the turbidity τ and the dry weight turbidity w in the estuary of Tokoro River.

$$N(D) = \frac{1}{\sqrt{2\pi} \cdot \sigma_1} e^{\left(-\frac{(D-\mu_1)^2}{2\sigma_1^2}\right)} + \frac{1}{\sqrt{2\pi} \cdot \sigma_2} e^{\left(-\frac{(D-\mu_2)^2}{2\sigma_2^2}\right)}, \cdots (7)$$

where μ_1 is the mode diameter of small particles, σ_1, is the standard deviation of small particles, μ_2 is the mode diameter of large particles, and σ_2 is the standard deviation of large particles. When formula (7) was matched to the counted number of particles shown in Figure 13 by the least squares method, this size distribution has two peaks, the optimal parameters of $\mu_1 = 5.0$, $\sigma_1 = 1.3$, $\mu_2 = 15.0$, and $\sigma_2 = 5.1$ were calculated. The bi-modal particle size distribution curve of these parameters is shown by a dotted line in Figure 13.

Figure 14 shows the change in the time dependent turbidity of surface water sampled in the estuary of Tokoro River on October 31, 2017, based on the method presented in section 2.2. From the observation results of particle distribution, a sedimentation velocity of two particles expressing a decrease in τ with time t was described as :

$$\tau = a_1 e^{\beta_1 t} + a_2 e^{\beta_2 t}, \cdots (8)$$

where α_1 and β_1 are the decreasing parameters of large particles and α_2 and β_2 are the decreasing parameters of small particles. The optimum value of formula (8) using the least squares method in relation to measured turbidity was shown as $\alpha_1 = 16.40$, $\beta_1 = -6.90 \times 10^{-3}$, $\alpha_2 = 24.09$ and $\beta_2 = -1.16 \times 10^{-1}$ in Figure 14. The τ calculated using formula (8) did not decline to 0.0, requiring 750 h (31 days) to reach < 0.1. If $\alpha_2 = 0$ was substituted, the τ of large particles only could be calculated, which required 70 h to reach < 0.1. Substituting the mode diameter 5.0 µm of small particles obtained the above results in the Stokes equation[29], where the average particle density was 1.11 g cm^{-3}. The terminal sedimentation velocity of small particles was 1.67×10^{-5} cm s^{-1} or 1.44×10^{-2} m day^{-1}. Similarly, the particle density of large particles was 1.13 g cm^{-3} with the mode diameter of 15.0 µm. The terminal sedimentation velocity of large particles was 1.77×10^{-4} cm s^{-1} or 1.53×10^{-1} m day^{-1}.

Table 2 Number of particles of suspended solids in the estuary of Tokoro River on October 31, 2017. D µm is particle diameter and, N_a is the number present in 100 particles and N_v is the number of particles in 1.0 L.

D µm	N_a	N_v
2.5 ± 0.5	10	1.05×10^8
3.5 ± 0.5	32	3.35×10^8
5.0 ± 0.5	54	5.66×10^8
8.7 ± 0.5	1	1.05×10^7
15.0 ± 0.5	2	2.10×10^7
20.9 ± 0.5	1	1.05×10^7
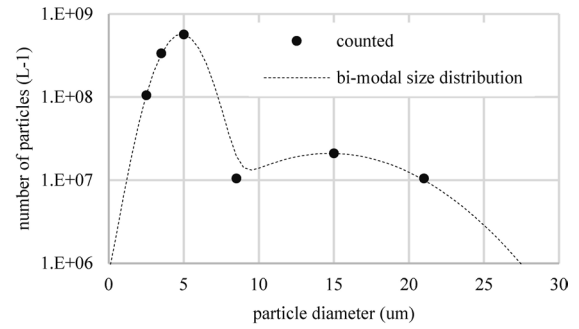
Fig. 13 Bi-modal particle size distribution of the suspended solids in the surface waters at the estuary of Tokoro River on October 31, 2017.
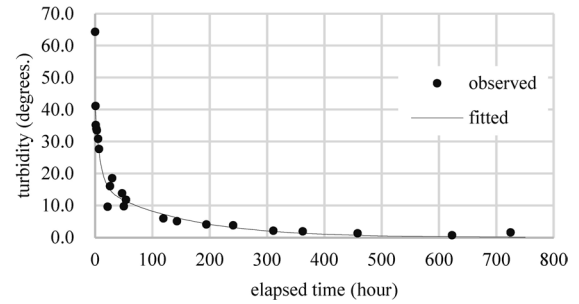
Fig. 14 Variation in the turbidity of the surface water of the estuary of Tokoro River over time on October 31, 2017. Solid line shows the approximate curve of the relationship between lapsed time and turbidity.

4. Discussion

In order to estimate turbidity τ from aerial drone images, the linear regression model and the exponential regression model, which were calculated from each pixel value of x_R, x_G, and x_B photographed with the drone, were provided and compared. In the case of the linear regression model, significant correlation was found between each x_R and x_G with respect to τ from the results of formula (1) and (2) in Section 3.2, but x_B in formula (3) was not significant for τ. Thus, x_B could not be used to estimate τ in the linear

regression model. The coefficient of determination between x_R and τ was 0.631, the coefficient of determination between x_B and τ was 0.474 ; That means the correlation between x_R and τ was larger than the correlation between x_G and τ. In addition, when x_R and x_G were linear combined shown in formula (4), there was a problem that the coefficient of the G channel became a negative value. The result shows that τ is difficult to express as the simple linear combination model of x_R and x_G. Therefore, when τ is expressed by the linear regression model, it is desirable to express only by x_R shown in formula (1). From Figure 10 B), it is obvious that x_B is not significant for τ even in exponential regression. In the case of the exponential regression model, significant correlation was found between each x_R and x_G with respect to τ from the results of formula (5). The RMSE when using x_R was 2.04 and the RMSE when using x_G was 4.81, so there was a 2.4 times difference in precision. For this reason, the two models consisted of only x_R. The RMSE of the linear regression model was 14.69 and the RMSE of the exponential curve model was 2.04, so the exponential curve model became valid. Since the expanded uncertainty of this model was $2\,RMSE = 4.08$, it is possible to estimate the environmental standard of rivers of 25 degrees for highly concentrated rivers. However, in order to detect turbidity of 2 degrees that is not affected by the fishery, the expanded uncertainty should be below 1.0, so the precision of this model is not enough. In order to estimate the low turbidity range, there should be an accumulation of observation data and increased precision in the future. On the other hand, the reason why a_G the coefficient of x_G became negative in spite of the x_G and τ small correlation could be that the multiple regression parameter a_G may have been adjusted to minimize RMSE. In general, inorganic suspended solids such as soils reflect red light more strongly than green light[30], but Chlorophyll a in phytoplankton has the opposite spectral characteristics due to photosynthesis[2]. Thus, in order to increase the precision of estimating τ, it is necessary to collect chlorophyll a concentration data.

Finally, the example of applying the w estimation model provided in formula (5) and (6) to drone observation over and around the estuary of the Tokoro river was examined. Table 3 shows pixel values in the white square area in Figs 6 and 7 and the estimated w calculated with formula (5) and (6) from the pixel value x_R. Figure 15 a) shows the distribution of w calculated by interpolation and extrapolation with GMT[31], a geographic information system, from the drone imagery on October 24, 2017. The difference in w between the inside and outside of the tidal boundary line was large at all three locations of Jonan Beach, the fishing village center and the east coast of the fishing port. The w inside the boundary line indi-

Table 3 stimated w calculated with the formula (5) and (6) from the x_R from sample areas from Figures 6 and 7. the value of w remains including the uncertainty RMSE ($=2.04$). The asterisk * represents when w was less than 2 RMSE. The double asterisk ** represents when w was less than RMSE. Black fills indicate $w>25$ and light gray fills indicate $w>2$.

date	location	test site	average pixel value x_R	estimated dry weight turbidity w
2017/10/24	estuary	E1	127.6	64.8
		E2	109.2	15.7
	off the Jonan beach	J1	134.4	111.1
		J2	123.0	45.2
		J3	37.4	0.8 **
	off the village center	V1	125.5	55.1
		V2	108.7	15.1
		V3	40.7	0.8 **
	east of the port	P1	123.0	45.1
		P2	49.5	0.8 **
2017/10/27	estuary	E3	90.3	4.1
		E4	94.7	5.5
	off the Jonan beach	J4	108.5	15.0
		J5	109.9	16.5
	off the village center	V4	80.2	2.2 *
		V5	71.4	1.4 **
	east of the port	P4	113.9	22.4
		P5	109.1	15.6

cated higher than the river environmental standard of 25 degrees at all three locations of Jonan Beach, the fishing village center and the east of the Tokoro fishing port. On the other hand, w inside the tidal boundary line indicated lower than 2 degrees of the coastal revetment standards at all three locations. In this result, on October 24, there were large differences in w between the high turbidity water area and other areas. The high turbidity area exceeding 25 degrees covered 28.5% of the sea area 7.2 km $\times$ 4.5 km ($32.0\,\mathrm{km}^2$) from the river estuary. The $w = 55.1$ degrees in the northern tidal boundary of the high turbidity area and $w = 45.1$ degrees in the eastern tidal boundary were slightly lower than $w = 64.8$ degrees in the vicinity of the estuary. However, $w = 111.1$ degrees in the western boundary was higher than the turbidity in the vicinity of the estuary. Figure 15 b) shows the distribution of the surface turbidity on October 27 calculated from the drone image similar to a). Compared to October 24, the w inside the tidal boundary line was lower than 25 degrees in all three places. The difference of the w between the outside and the inside of the tidal boundary line became small in all places. However, the value of the $w = 16.5$ degrees in the offshore of Jonan Beach and $w = 22.4$ degrees in the eastern offshore of Tokoro fishing port indicated higher values than the value of the $w = 5.5$ degrees in the vicinity of the estuary. From these observation examples, there were 2.8 times a clear difference between the average surface turbidity 50.3 degrees in the high turbidity area

on October 24 after passing the low pressure and the surface turbidity 17.7 degrees after 3 days.

Since the time for large particles to settle from the surface layer is 70 hours from the result from section 3.4, the large particles supplied from the Tokoro River in these three days are considered to have settled immediately from the surface layer. The sedimentation flux of large particles was $18.57 \, \mathrm{g \, m^{-2} \, day^{-1}}$ on October 24, 2017 and $19.74 \, \mathrm{g \, m^{-2} \, day^{-1}}$ October 31. Each flux was calculated by multiplying w in Table 1 by the terminal sedimentation velocity. The w on October 24 was converted from turbidity and formula (6). The sedimentation flux in these cases are almost twice as fast as the previously known the normal state sedimentation flux of $9.24 \, \mathrm{g \, m^{-2} \, day^{-1}}$ offshore of Lagoon Notoro-ko[32]. However, the difference between the inside and outside of the tidal boundary line was small on October 27. It is reported that the suspended solids derived from rivers are mixed with seawater slowly after diffusing to the surface once[33]. The small particles could stay on the surface for more than 31 days, from the result of section 3.4, so the small particles remaining on the sea surface are considered to have mixed with seawater and diffused across the tidal boundary line. This drone observation seems to have captured the diffusion of the suspended solids before and after being mixed with seawater in the surface layer.

The estuary of the Tokoro River faces the northeast as shown in Figure 2 and the Soya Warm Current flows toward the east on the north side of the estuary. Under this condition, suspended solids should flow northeast. However, the results shown in Table 3 indicated that the turbidity on the west side was higher than the turbidity of the vicinity of the estuary, the source of suspended solids. There is a shore reef on the shallow sea floor just east of the estuary, and the flow of the river is blocked by this shore reef, once heading west, then heading to north[34]. For this reason, it is considered that suspended solids flowing from the estuary stayed in the vicinity of the western tidal boundary line. The cause of the higher turbidity in the vicinity of the west boundary line than the turbidity of the estuary cannot be identified, but there may be factors other than the influence of suspended solids from the estuary because of the nearness to the inlet of the Lagoon Notoro-ko.

It is difficult to observe such as these two above instantaneous phenomena with satellites and ship observation. In order to take advantage of the convenience of drone observation for environmental monitoring of the coastal area around this estuary in the future, real-time calculation of the turbidity estimation model and continuous shooting with movies will be necessary.
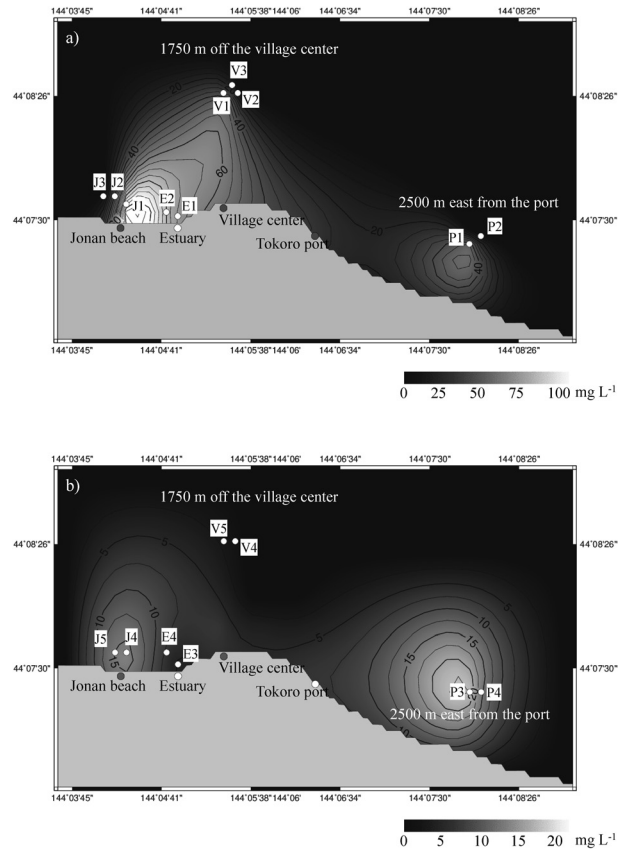

Fig. 15 Surface distribution of w calculated using the GMT from the drone imagery. a) On October 24, 2017. b) On October 31, 2017.

Acknowledgement

References

1) Hokkaido Government, Profile of Hokkaido Fisheries, <http://www.pref.hokkaido.lg.jp/sr/sum/grp/02/AP_05_2010_Fisheries_in_Hokkaido.pdf> (Last Access May 29, 2018)

2) Lalli C and Parsons T (1997) Biological Oceanography : An Introduction, Second Edition. Elsevier Butterworth Heinemann, Oxford, pp. 40–73.

3) Aota M (1971) Study of the Variation of Oceanographic Condition to the North East off Hokkaido in the Sea of Okhotsk III. *Low Temp. Sci. Ser. A Phys. Sci.* **29** : 210–224.

4) Takizawa T (1982) Characteristics of the Soya Warm Current in the Okhotsk Sea. *J. Ocea. Soc. J.* **38** : 281–292.

5) Aota M, Ishikawa M and Uematsu E (1988) Variation in Ice Concentration off Hokkaido Island. *Low Temp. Sci. Ser. A Phys. Sci.* **47** : 161–175.

6) Maita Y and Toya K (1986) Characteristics on the Distribution and Composition of Nutrients in Subarctic Regions. *Bull. J. Soc. Fish. Ocea.* **50** (2) : 105–113.

7) Kudo I, Frolan A, Takata H and Kobayashi N (2011) Ocean-

ographic Structure and Biological Productivity in the Coastal Area of Okhotsk Sea. *Bull. Coast. Ocea.* **49** (1) : 13–21.

8) Hokkaido Regional Development Bureau, Ministry of Land, Infrastructure, Transport and Tourism Japan <https://www.hkd.mlit.go.jp/ab/tisui/v6dkjr00000006jx.html>

9) WOTTON R S, MALMQVIST B (2001) Feces in Aquatic Ecosystems : Feeding Animals Transform Organic Matter into Fecal Pellets, which Sink or are Transported Horizontally by Currents ; these Fluxes relocate Organic Matter in Aquatic Ecosystems. *BioScience* **51** (7) : 537–544.

10) YAMAMOTO G (1956) On Behavior of the Scallop under some Environmental Conditions, with Special Reference to Effects of Suspended Silt, Lack of Soluble Oxygen and others on Ciliary Movement of Gill Pieces. *J. J. Ecol.* **5** (4) : 172–175.

11) Japan Meteorological Agency, Latest Weather, <https://www.data.jma.go.jp/fcd/yoho/typhoon/statistics/landing/landing.html>

12) KITANO Y and YAMADA T (2016) The Relationship between Explosive Cyclone through Northern Japan and Pacific Blocking. *J. J. Soc. Civil Eng. Ser. B1* **72** (4) : 121–126.

13) Kyusyu Univ., Explosive Cyclone Database, <http://fujin.geo.kyushu-.ac.jp/meteorol_bomb/index.php>

14) Weekly Paper Suisan Shinbun, <http://suisan.jp/article-7483.html> (Last access November 20, 2017).

15) Ministry of Agriculture, Forestry and Fisheries, <http://www.maff.go.jp/j/saigai/typhoon/20171106.html> (Last access November 20, 2017)

16) Fishing Communities Promotion and Disaster Prevention Division, Fisheries Infrastructure Department, Fisheries Agency Japan, <http://www.jfa.maff.go.jp/j/bousai/hamaplan/hokkaido_koikihamaplan.html> (Last access November 20, 2017)

17) FUKUSHIMA H, KASHIWAMURA M, YAKUWA I and TAKAHASHI S (1964) A Study of the mouth of the Ishikari river. *Proc. Coast. Eng. Comm. J. Soc. Civil Eng.* **11** : 137–146.

18) FUNAKI J and SHINME R (1999) Sediment diffusion from Mukawa River to ocean after the 1997 Flood. *Proc. Conf. Hydr. Eng. J. Soc. Civil Eng.* **43** : 449–454.

19) ASAKUMA K, KENJYOU Y and SHIMA T (2016) Study of the classification method for the costal water in an outfall area along the Hokkaido coast in the Okhotsk Sea from satellite imagery. *Low Temp. Sci.* **74** : 85–93.

20) OHMINATO T, KANEKO T, KOYAMA T, WATANABE A, YASUDA A, TAKEO M, HONDA Y and IGUCHI M (2011) Volcano Observations Using an Unmanned Autonomous Helicopter : seismic observations near the active summit vents of Sakurajima volcano, Japan. *Geophys. Res. Abst.* **13** : EGU2011-2855.

21) KOYAMA T, KANEKO T, OHMINATO T, YANAGISAWA T, WATANABE A and TAKEO M (2013) An aeromagnetic survey of Shinmoedake volcano, Kirishima, Japan, after the 2011 eruption using an unmanned autonomous helicopter. *Earth Planets Space* **65** : 657–666.

22) NIETHAMMER U, JAMES M R, ROTHMUND S, TRAVELLETTI J and JOSWIGA M (2012) UAV based remote sensing of the Super-Sauze landslide: Evaluation and results. *Eng. Geology* **28** (9) : 2–11.

23) LOMAX A S, CORSO W and ETRO J F (2005) Employing Unmanned Aerial Vehicles (UAVs) as an element of the Integrated Ocean Observing System. *Proc. OCEANS 2005 MTS/IEEE* **1** : 184–190.

24) KLEMAS V V (2015) Coastal and Environmental Remote Sensing from Unmanned Aerial Vehicles : An Overview. *J. Coastal Res.* **31** (5) : 1260–1267.

25) PRAVEEN C, MARCELO B, DAVID K and CORRAL J V (2015) A Tone mapping operator based on Neural and Psychophysical Models of Visual Perception. *Proc. SPIE 9394, Human Vision and Electronic Imaging XX* : 93941I.

26) Overseas Environmental Cooperation Center, Japan, <https://www.env.go.jp/earth/coop/coop/document/04-wpctmj1/04-wpctmj1.pdf> (Last Access December 11, 2017)

27) Ministry of the Environment Government of Japan, Environmental Standard about Preservation of Living Environment <https://www.env.go.jp/kijun/pdf/wt2-1-1.pdf>

28) YONG H K, JUNGHO I, HO K H, JONG-KUK C and SUNGHYUN H (2014) Machine learning approaches to coastal water quality monitoring using GOCI satellite data. *GIScience & Remote Sens.* **51** (2) : 158–174.

29) MOURI M and FUJII S (1997) Analysis on settling velocity distribution of suspended matter determined by the Plural Settling Cylinders Method. *J. J. Soc. Water Env.* **20** (12) : 838–844.

30) California Institute of Technology, The ECOSTRESS spectral library, <https://speclib.jpl.nasa.gov/>

31) GMT-The Generic Mapping Tools, <http://gmt.soest.hawaii.edu/> (Last Access April 21, 2018)

32) MIYAZONO A, TADA M and KOMATSU T (1995) Growth of Scallops (*Patinopecten yessoensis*) in sowing culture grounds around the Abashiri Bay in relation to water and sediment flux. *Bull. J. Soc. Fish. Ocea.* **59** (4) : 389–397.

33) ISHII J, OKADA S and IWATA K (1977) The Suspended Matter in Sea Water in the Bay of Ishikari, Hokkaido, North Japan. *Earth Sci.* **31** (1) : 19–33.

34) YAMASHITA T, OSHIDA R, TOMISAWA S, SATO M, TOKISAWA T and YAMAGAMI Y (2014) Influence of the Climate Change on Sediment Transport around the Second Inlet of Saroma Lake. *J. J. Soc. Civil Eng. Ser. B2* **70** (2) : 606–610.

航空ドローンを用いた沿岸域懸濁物監視手法の開発：
低気圧イベント後における北海道常呂川
河口周辺のケーススタディ

朝隈康司*†・大宮千尋*・喜田直人*・北村充彰**

要約：オホーツク海北海道沿岸地域はホタテ貝の養殖が盛んであるが，この地域を流れる河川から，低気圧イベントなどの後に供給される懸濁物による被害が問題となってきている。このため簡便で広範囲の懸濁物をモニタリングする方法の開発が望まれている。本研究は，道東常呂町を流れる常呂川の河口域を対象として，特殊な装置を必要としない航空ドローン搭載カメラのみによる濁度モニタリング方法を開発することを目的とする。計測用ではない一般向けカメラの特性は非公開の場合が多く，このようなカメラを計測に用いるには，その特性を対象物に合わせて解析する必要がある。本手法では，常呂川の河口で濁水を採水し，採水箇所でドローンをホバリングさせ河川表面を撮影し，撮影された画像と標準白板から河川表面の反射率を算出して，反射率と濁度の関係を線形回帰モデルと指数回帰モデルで比較した。線形回帰モデルの RMSE および指数回帰モデルでの RMSE を比較した結果，このドローンに搭載されたカメラは指数回帰モデルを用いた場合に濁度の再現性が高いことがわかった。しかしながら，本手法の精度は，河川の定常状態での低濁度を監視するには不十分である。検出精度を向上させるためには，植物プランクトンなどの有機懸濁物との同時観測が必要である。

キーワード：濁度，懸濁物，航空ドローン，オホーツク海

* 東京農業大学生物産業学部アクアバイオ学科
** 東京農業大学大学院生物産業学研究科アクアバイオ専攻
† Corresponding author（E-mail：k-asakum@ nodai.ac.jp）